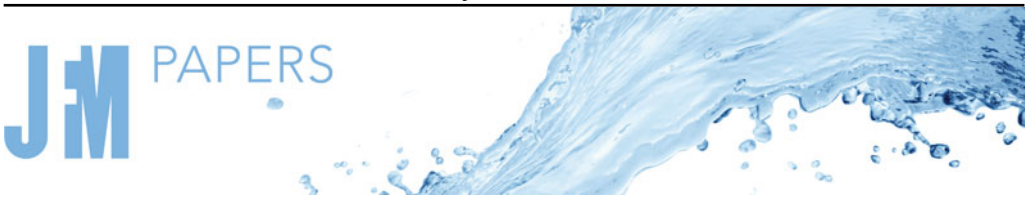
J. Fluid Mech. (2025), *vol.* 1016, A67, doi:10.1017/jfm.2025.10451



Particle dynamics and dune formation in Rayleigh–Bénard convection: a particle-resolved simulation study

Xianyang Chen[1,2], **Rodolfo Ostilla-Mónico**[3], **Daniel Floryan**[1], **Myoungkyu Lee**[1] **and Andrea Prosperetti**[1,4,5]

[1]Department of Mechanical and Aerospace Engineering, University of Houston, Houston, TX 77204, USA

[2]School of Aerospace Engineering and Applied Mechanics, Tongji University, Shanghai 200092, PR China

[3]Departamento de Ingeniería Mecánica y Diseño Industrial, Escuela Superior de Ingeniería, Universidad de Cádiz, Puerto Real 11519, Spain

[4]Faculty of Science and Technology, University of Twente, Enschede 7500 AE, The Netherlands

[5]Department of Mechanical Engineering, Johns Hopkins University, Baltimore, MD 21218, USA

Corresponding authors: Xianyang Chen, tomchen95@tongji.edu.cn; Daniel Floryan, dfloryan@uh.edu

(Received 3 March 2025; revised 5 July 2025; accepted 7 July 2025)

This paper presents numerical results for Rayleigh–Bénard convection with suspended particles at Rayleigh numbers $Ra = 10^7$ and 10^8, and unit Prandtl number. Accounting for their finite size makes it possible to investigate in detail the mechanism by which the particles, which are 10 % heavier than the fluid, get resuspended after settling, thus maintaining a two-phase circulating flow. It is shown that an essential component of this mechanism is the formation of particle accumulations, or 'dunes', on the bottom of the Rayleigh–Bénard cell. Ascending plumes become localised on these dunes. Particles are dragged up the dune slopes, and when they reach the top, are entrained into the rising plumes. Direct resuspension of particles from the cell bottom, if it happens at all, is very rare. For $Ra = 10^7$, aspect ratios (width/height) $\Gamma = 1, 2, 4$ are considered. It is found that in these and in the other cases simulated, at steady state, a single dune evolves, the largest linear dimension of which is comparable to the cell size. A remarkable consequence is that even at the low volume fraction considered here, 3.27 %, the particles are able to structure the flow and to determine the size and position of the largest ascending plumes. Their effect on the Nusselt number, however, remains small. This and other results are explained on the basis of the ratio of the cell-bottom viscous boundary-layer thickness to the particle diameter.

Key words: particle/fluid flow, Bénard convection

© The Author(s), 2025. Published by Cambridge University Press.

https://doi.org/10.1017/jfm.2025.10451 Published online by Cambridge University Press

1. Introduction

Rayleigh–Bénard convection with suspended particles occurs in a variety of natural and industrial environments, including air circulation in rooms and built spaces (see e.g. Balachandar *et al.* 2020; Rayegan *et al.* 2023), oceans and the atmosphere (see e.g. Stein *et al.* 2015; Auta, Emenike & Fauziah 2017), metal production processes (see e.g. Jarvis & Woods 1994), and magma chambers along with other planetary processes (see e.g. Elkins-Tanton 2012). The settling of particles heavier than the suspending fluid is an important process in such systems, but so is the much less studied converse process of particle resuspension. For example, the differentiation of crystals in magma chambers and in the solidification of metal alloys is the result of a competition between sedimentation and resuspension (see e.g. Martin & Nokes 1989; Solomatov, Olson & Stevenson 1993; Jarvis & Woods 1994; Elkins-Tanton 2012). As another example, the effectiveness of oceanic sediments as sinks for microplastic particles is also critically dependent on the resuspension rate of the microplastic debris (see e.g. Cózar *et al.* 2017).

Despite its importance, the microphysics of particle resuspension in natural convection has not been studied in great detail. Until very recently, an important experimental observation by Solomatov *et al.* (1993), according to which resuspension occurs from bottom particle accumulations, or dunes, has been cited only sporadically in the literature (see e.g. Lavorel & Le Bars 2009). A numerical study of this mechanism must account for the finite size of the particles because once a point-particle is deposited on the bottom of the domain, owing to the no-slip condition, it finds itself immersed in a quiescent fluid and cannot be resuspended. For this reason, earlier point-particle studies have been forced either to consider the transient version of the problem (see e.g. Lavorel & Le Bars 2009; Patočka *et al.* 2020) or to maintain a statistically steady situation by artificially re-injecting the particles above the bottom surface once they settled. Particles were re-injected at the top plate in some studies (see e.g. Oresta & Prosperetti 2013; Oresta, Fornarelli & Prosperetti 2014), while in others they were re-injected in the bottom 10 % of the cell (see e.g. Park, O'Keefe & Richter 2018). Neither procedure is very satisfactory as they artificially add energy to the system, preventing the study of the pure effect of particles on the fluid circulation. The procedure of Park *et al.* (2018) minimises this artefact, but it has the consequence that only very light particles, with terminal velocity approximately 1 % of the convection free-fall velocity (see (2.7) below for a definition), could remain in suspension, while heavier ones kept settling and being re-injected, circulating near the bottom of the cell. Other authors, who studied the so-called vertical natural convection, in which the circulation is established between two vertical plates maintained at different temperatures, faced the same problem and handled it in similar ways, allowing the particles to settle (see e.g. Puragliesi *et al.* 2011) or artificially re-injecting them (see e.g. Gereltbyamba & Lee 2018). Here, we focus on the mechanism described by Solomatov *et al.* (1993), and study in detail the mechanism of dune formation by means of particle-resolved numerical simulations. We illustrate the crucial role that dunes play in the particle resuspension mechanism and in the restructuring of the convective flow.

The present work is a continuation of two previous studies in which particle-resolved simulations of particle resuspension in Rayleigh–Bénard convection were limited to a Rayleigh number $Ra = 10^7$ and a cubic computational domain characterised by an aspect ratio (width over height) $\Gamma = 1$, namely Chen & Prosperetti (2024) and Chen *et al.* (2024). In this paper, we extend the previous work to investigate the effect of cell aspect ratios $\Gamma = 1, 2, 4$ for $Ra = 10^7$ and $\Gamma = 2$ for $Ra = 10^8$. Interest in larger aspect ratios is motivated, among others, by recent studies of single-phase Rayleigh–Bénard convection that have highlighted the importance of large-aspect-ratio domains, showing that the

https://doi.org/10.1017/jfm.2025.10451 Published online by Cambridge University Press

largest scales in the flow increase in size with increasing aspect ratio up to $\Gamma = 64$ (see e.g. Stevens *et al.* 2018; Krug, Lohse & Stevens 2020; Shishkina 2021; Lee 2024).

Besides the present one, dunes arise in several other contexts, such as on river bottoms (see e.g. Best 2005; Kidanemariam & Uhlmann 2014; Fry *et al.* 2024) and on sand deserts (see e.g. Pye & Tsoar 2009; Kok *et al.* 2012). In both cases, the flow is primarily unidirectional, and the longitudinal profile of the dunes is approximately triangular, with a milder upstream slope and a steeper downstream slope, leading to flow separation at the crest, and generating turbulence downstream. Particles are moved uphill and deposited on the downstream side, leading to a slow, continuous, downstream migration of the dune (see e.g. Engelund & Fredsøe 1982). Shear stress on the bed surface is the main mechanism for the erosion of underwater dunes, either by pushing sedimented particles uphill or directly suspending them with high turbulent stresses. In contrast, the erosion of sand dunes in air, where the density difference is much larger, is mainly due to saltation, in which particles hop along the surface and eject additional particles upon impact with the surface (see e.g. Kok *et al.* 2012).

The crucial difference between dunes in deserts and river beds and the situation considered here is that in Rayleigh–Bénard convection, the flow is organised in a system of circulating cells. A rising plume at the boundary between two contiguous cells is formed by flow reaching its base from opposite directions. For this reason, bottom particles form a dune by accumulating along the plume base. We find that due to their contact with the hot base, the dunes are warm, and strengthen and redistribute the rising plumes above them. Thus they are not only the passive outcome of the circulating flow, but affect it directly.

Only a few studies have utilised particle-resolved simulations in scenarios involving sediment beds (see e.g. Kidanemariam & Uhlmann 2014; Vowinckel *et al.* 2021). The situation is similar for Rayleigh–Bénard convection. Demou *et al.* (2022) used a modification of Uhlmann's immersed boundary method to simulate particle-resolved flows with $Ra = 10^8$ and $\Gamma = 2$ in cells with height between 10 and 20 particle diameters. These parameters are comparable to ours, although their Prandtl number, $Pr = 7$, is greater than ours, $Pr = 1$. They used periodicity conditions in the horizontal direction, as we do. A significant difference, however, is that while our particles are 10 % heavier than the fluid, theirs are neutrally buoyant at the mean fluid density, and therefore heavier than the fluid near the bottom, and lighter near the top. This circumstance, coupled with the large volume fractions ϕ in which these authors were mostly interested (mostly $\phi = 10\,\%$, $20\,\%$, $30\,\%$ and $40\,\%$), caused the formation of dense particle layers near the bottom and top walls, which prevented the formation of dunes. Furthermore, their focus was on the effect of particles on turbulence and the heat transfer through the cell rather than resuspension. In the present study, we limit ourselves to a much smaller volume fraction, 3.27 %, and show that due to the formation of dunes, even this small number of particles is sufficient to cause a major reorganisation of convection in the cell. From their figure 6, the Nusselt number for $\phi = 5\,\%$ is approximately 32, quite comparable to ours, which is approximately 31 and exhibits the same very slight increase from the single-phase case. In another recent paper, Wu *et al.* (2024) carried out particle-resolved simulations with a lattice Boltzmann method for $Ra = 10^7$, $Pr = 0.71$ and ϕ up to 9 %. As in the study of Demou *et al.* (2022), their particles were neutrally buoyant, but unlike Demou *et al.* (2022) and the present work, their vertical boundaries were adiabatic. Their cell had a rectangular cross-section and aspect ratio $\Gamma = 1$ on the basis of the longer horizontal dimension. Their paper focuses on the numerical method and also presents some results on the effect of particles on the fluid mechanics of the problem, such as velocity and energy spectra. For $\phi = 0$ and 3 %, they

https://doi.org/10.1017/jfm.2025.10451 Published online by Cambridge University Press

find Nusselt numbers approximately 16.2 and 16.6, respectively, which are very close to ours, which is approximately 16.5 for both single- and two-phase flow with $\Gamma = 2$. While the available results are admittedly sparse, a strong conclusion suggested by the different parameter values and simulation conditions of our study and those by Demou *et al.* (2022) and Wu *et al.* (2024) is that, at least for volume fractions up to a few per cent, the effect of particles on the Nusselt number is small. The flow reorganisation that we illustrate can, however, have other interesting consequences, e.g. for the spatial distribution of fractional or homogeneous crystallization of the liquidus phase of molten rocks and metals.

A final example of particle-resolved simulations in particulate natural convection is the work by Kajishima and co-workers (see e.g. Takeuchi *et al.* 2015; Gu, Takeuchi & Kajishima 2018). These authors were interested in lower Rayleigh numbers, in the range $10^4 - 10^6$, and particle thermal conductivities so large that a significant amount of heat was transferred on collision, and heat transfer by conduction amounted to a significant contribution to the overall heat transfer through the cell. They also mostly considered very dense suspensions, with volume fractions up to, and in excess of, 50 %. Their particles were either neutrally buoyant or, at most, 0.5 % denser than the fluid. These parameters are so different from ours that no comparison with their work is possible.

2. Methods

2.1. *Governing equations and non-dimensional numbers*

We work with the standard Rayleigh–Bénard set-up, where fluid is confined between a hot bottom wall and a cold top wall at fixed temperatures T_h and T_c, respectively. The governing equations for the fluid follow the Boussinesq approximation (see e.g. Ahlers, Grossmann & Lohse 2009):

$$\boldsymbol{\nabla} \cdot \boldsymbol{u} = 0, \tag{2.1}$$

$$\partial_t \boldsymbol{u} + \boldsymbol{u} \cdot \boldsymbol{\nabla} \boldsymbol{u} = -\frac{1}{\rho_0} \boldsymbol{\nabla} p + \nu_f \nabla^2 \boldsymbol{u} + [1 - \beta(T - T_0)] \boldsymbol{g}, \tag{2.2}$$

$$\partial_t T + \boldsymbol{u} \cdot \boldsymbol{\nabla} T = D_f \nabla^2 T. \tag{2.3}$$

Here $\boldsymbol{u}$, p and T are the fluid velocity, pressure and temperature, respectively, $\boldsymbol{g}$ is the vector acceleration of gravity, β is the thermal expansion coefficient, ν_f and D_f are the kinematic viscosity and thermal diffusivity, respectively, $T_0 = (1/2)(T_h + T_c)$ is the reference temperature, and ρ_0 is the fluid density at T_0.

The particles are assumed to be equal spheres of diameter d_p. Their motion is governed by Newton's law, accounting for gravitational, hydrodynamic and collision forces. The lumped-capacitance approximation is used for the particle temperature. Since the fluid velocity, pressure and temperature in the neighbourhood of each particle are fully resolved, the hydrodynamic forces and heat fluxes can be explicitly calculated without recourse to correlations; the calculation of these quantities is described in Sierakowski & Prosperetti (2016) and Chen & Prosperetti (2024).

It is convenient to introduce a reference particle Reynolds number $Re_p = d_p u_p / \nu_f$, which we define in terms of the terminal velocity u_p of a spherical particle in a fluid of density ρ_0 at rest. This quantity is determined implicitly by a balance of the gravity and drag forces, the latter expressed in terms of a drag coefficient $C_D = C_D(Re_p)$:

$$\frac{\pi}{4} d_p^2 C_D(Re_p) \frac{1}{2} \rho_0 u_p^2 = \frac{\pi}{6} d_p^3 (\rho_p - \rho_0) g. \tag{2.4}$$

https://doi.org/10.1017/jfm.2025.10451 Published online by Cambridge University Press

Here, ρ_p is the particle density, and $g = \|\boldsymbol{g}\|$; for the drag coefficient, we use the well-known Schiller–Naumann correlation (see e.g. Clift, Grace & Weber 1978), namely $C_D = (24/Re_p)(1 + 0.15\, Re_p^{0.687})$. A particle mechanical relaxation time can then be defined by

$$\tau_p = \frac{m_p}{3\pi d_p \rho_0 \nu_f \left(1 + 0.15 Re_p^{0.687}\right)} = \frac{(\rho_p/\rho_0) d_p^2}{18\nu_f \left(1 + 0.15 Re_p^{0.687}\right)}, \tag{2.5}$$

with m_p the particle mass. A reference thermal particle relaxation time can be similarly defined in terms of a particle Nusselt number for which we use the correlation $Nu_p = 2(1 + 0.3\, Pr^{1/3} Re_p^{1/2})$ (see e.g. Ranz & Marshall 1952; Clift *et al.* 1978; Bergman *et al.* 2018):

$$\tau_{p,th} = \frac{\rho_p c_{pp} d_p^2}{12 k_f \left(1 + 0.3\, Pr^{1/3} Re_p^{1/2}\right)} = \frac{(\rho_p/\rho_0)(c_{pp}/c_{pf}) d_p^2}{12 D_f \left(1 + 0.3\, Pr^{1/3} Re_p^{1/2}\right)}, \tag{2.6}$$

with c_{pp} and c_{pf} the particle and fluid specific heats, and k_f the fluid thermal conductivity.

When the fluid equations (2.1), (2.2) and (2.3) are non-dimensionalised in terms of ρ_0, the cell height H and the free-fall velocity, given by

$$U_f = \sqrt{g\beta(T_h - T_c)H}\,, \tag{2.7}$$

only two dimensionless parameters are left, the Rayleigh and Prandtl numbers, defined by

$$Ra = \frac{\beta(T_h - T_c) g H^3}{\nu_f D_f}, \quad Pr = \frac{\nu_f}{D_f}. \tag{2.8}$$

In particular, the dimensionless time becomes $t^* = t/\tau_f$, with $\tau_f = H/U_f$ the circulation time scale in the cell. The particle mechanical and thermal Stokes number are defined by

$$St = \frac{\tau_p}{\tau_f} = \frac{U_f \tau_p}{H}, \quad St_{th} = \frac{\tau_{p,th}}{\tau_f}. \tag{2.9}$$

An important point to note is that the presence of particles introduces additional dimensionless parameters that depend on some of the same physical quantities that appear in the definitions of Ra and Pr. Thus, for example, while in a single-phase Rayleigh–Bénard simulation doubling either $\beta(T_h - T_c)$ or g would result in the doubling of Ra and have an identical effect on the flow (once expressed in the proper dimensionless variables), in the present two-phase case the effect would be different, as with the second choice the particle Reynolds number would be affected, and with it the dynamics of the flow. It is necessary to keep this fact in mind for the proper interpretation of the results described in the next section.

2.2. *Computational method and set-up*

The cell used for the simulations has a square base with side L and height H. The aspect ratio is defined by

$$\Gamma = \frac{L}{H}. \tag{2.10}$$

Following a method common in the literature to approximate the simulation of natural convection in cells larger than those that can be handled by the available computational resources, periodicity boundary conditions are used in the horizontal directions (see e.g.

https://doi.org/10.1017/jfm.2025.10451 Published online by Cambridge University Press

Lohse & Shishkina 2024); no-slip and prescribed temperature conditions are imposed on the top and bottom surfaces, and no-slip conditions on the particle surfaces. A system of Cartesian coordinates is used, with x and y the horizontal coordinates, and z, oriented oppositely to the direction of $\boldsymbol{g}$, normal to the bottom and top surfaces; $z = 0$ corresponds to the bottom of the cell, so $0 \leqslant z \leqslant H$.

The particle-resolved simulations are carried out using the Physalis method, which has been thoroughly described and validated in several earlier publications (see, among others, Sierakowski & Prosperetti 2016; Wang, Sierakowski & Prosperetti 2017). The basic idea is that within a thin layer close to the particle surface, the fluid momentum and energy equations can be linearised, and the time derivatives neglected. With these steps, general analytical solutions, expressed as series of spherical harmonic functions multiplied by undetermined coefficients, become available for the velocity, pressure and temperature fields in each sphere's rest frame. After suitable truncation, these expressions are used to replace the boundary conditions on the particle's surface by equivalent conditions on the nearest Cartesian grid nodes, thereby avoiding difficulties associated with the complex geometrical relationship between spherical particles and the underlying fixed Cartesian grid. The undetermined coefficients of the series expansions are obtained by iteration. By this procedure, the no-slip and uniform-temperature conditions on the particle surfaces are imposed to analytical accuracy.

As shown in the earlier papers cited, and others, this method guarantees an accurate representation of the fields even with comparatively coarse discretisations. In the present paper, we use eight nodes per particle radius, and mostly truncate the spherical harmonics expansion to $\ell = 3$. The results of Sierakowski & Prosperetti (2016) show that with these choices, the motion of particles at Reynolds numbers as large as four times the ones of present concern can be calculated accurately. Furthermore, the number of degrees of freedom per particle is just the number of coefficients of the spherical harmonics used to represent the local solutions, and is therefore much smaller than the hundreds of degrees of freedom per particle typical of immersed boundary methods. Particle–particle and particle–wall collisions are handled by a soft-particle contact-force model (Sierakowski & Prosperetti 2016). Inside the dunes, fluid and particles are nearly motionless. In this case, the way in which the coefficients of the spherical harmonics expansions are calculated essentially amounts to a smooth extrapolation of the slow interstitial fluid velocity into the neighbouring particles. To speed up convergence of the iterations, in these situations the series are truncated to $\ell = 1$, making an efficient use of the information on the weak flow around the particle.

A uniform Cartesian grid is applied in all directions. The simulations are started keeping the particles fixed at random positions while the flow is established. Once statistical properties, such as the Nusselt number, have stabilised, the particles are released and begin to interact with the flow as they settle; the initial time $t = 0$ is counted from this moment. Table 1 presents numerical values of the dimensionless parameters and other quantities characterising the simulations.

For each one of the five simulations described in this study, the relative error in the total energy balance was less than 1 %. We have verified the correct implementation of periodicity boundary conditions on the side walls by translating the entire flow field arbitrarily in the horizontal direction, confirming that the formation of a dune near the side boundary that we sometimes observe is a random occurrence. The most demanding simulation carried out in the present study used 2.1 billion grid points and used 600 NVIDIA V100 GPUs on the Summit system at the Oak Ridge National Laboratory for approximately 63 days.

https://doi.org/10.1017/jfm.2025.10451 Published online by Cambridge University Press

Ra	Γ	H/d_p	ρ_p/ρ_0	u_p/U_f	Re_p	St	St_{th}	N_p	$N_x \times N_y \times N_z$
10^7	1	20	1.1	0.063	10.0	0.28	0.29	500	$320 \times 320 \times 320$
10^7	2	20	1.1	0.063	10.0	0.28	0.29	2000	$640 \times 640 \times 320$
10^7	4	20	1.1	0.063	10.0	0.28	0.29	8000	$1280 \times 1280 \times 320$
10^8	2	43.2	1.1	0.043	10.0	0.19	0.29	20 000	$1620 \times 1620 \times 810$
10^7	1	28.3	1.283	0.090	10.0	0.16	0.17	1413	$450 \times 450 \times 450$

Table 1. The parameters used for the five simulations discussed in this paper: $N_x \times N_y \times N_z$ is the grid resolution used in each direction, and N_p is the total number of finite-sized particles. In all the simulations, the Prandtl number is kept at $Pr = 1$.

3. Results

As noted in the previous section, the complete specification of a particulate Rayleigh–Bénard flow requires more parameters than the single-phase analogue, which renders it impossible to carry out an exhaustive exploration of parameter space, given the computationally intensive nature of each one of our simulations. We have chosen to focus primarily on the effect of the domain aspect ratio $\Gamma = L/H$, which we have varied by keeping the domain height H fixed so as to have $Ra = 10^7$, while taking the horizontal extent L of the domain equal, in turn, to H for $\Gamma = 1$, $2H$ for $\Gamma = 2$, and $4H$ for $\Gamma = 4$. In these simulations, the particle size and density were also kept constant at $H/d_p = 20$ and $\rho_p/\rho_0 = 1.1$, respectively. We were able to carry out two other simulations, one with $Ra = 10^8$, and one with smaller particles at $Ra = 10^7$. For the former, we increased H by a factor $10^{1/3} \approx 2.154$, keeping the same particle size as before, so that $H/d_p = 43.1$; the aspect ratio was set at $\Gamma = 2$, and the particle density was kept fixed at $\rho_p/\rho_0 = 1.1$. For the simulation with smaller particles at $Ra = 10^7$, for which we took $\Gamma = 1$, the cell height was kept fixed at the earlier value, but the particle diameter was decreased so that $H/d_p = 28.3$. In order to maintain the same buoyancy force as for the other $Ra = 10^7$ simulations, thereby preserving the value of the particle Reynolds number, in this last case, the particle density was increased to $\rho_p/\rho_0 = 1.283$.

For all the simulations, the fluid Prandtl number was kept fixed at $Pr = 1$, the ratio of specific heats at $c_{pp}/c_{pf} = 1$, and the particle volume fraction at $\phi = 3.27\ \%$. This required 500 particles for $\Gamma = 1$, 2000 for $\Gamma = 2$, and 8000 particles for $\Gamma = 4$. The increased cell volume for the $Ra = 10^8$ simulation required 20 000 particles, while 1413 were used for the smaller-particle simulation with $\Gamma = 1$. While the volume fraction for this last simulation was the same as for all the others, the mass fraction was approximately 16 % larger due to the increased mass of the particles.

Similarly to the studies of Demou *et al.* (2022) and Wu *et al.* (2024), in choosing these parameter values we have tried not to simulate specific physical systems, but to explore a region of parameter space in which we could expect some interesting physics while maintaining computational tractability. To relate our parameters to real systems, we may note that a particle that is 10 % heavier than water with Reynolds number 10 would have diameter approximately 682 μm, while a particle that is 10 % heavier than air at normal conditions would have diameter 4.15 mm. Cells with $H/d_p = 20$ would have heights 13.6 and 83 mm, respectively, and setting up Rayleigh number 10^7 or 10^8 in them would be a highly non-trivial experimental challenge. Approaching practical systems on which accurate experiments can be carried out would require values of H/d_p at least one order of magnitude greater, and would be impossible with the computational resources available today.

https://doi.org/10.1017/jfm.2025.10451 Published online by Cambridge University Press

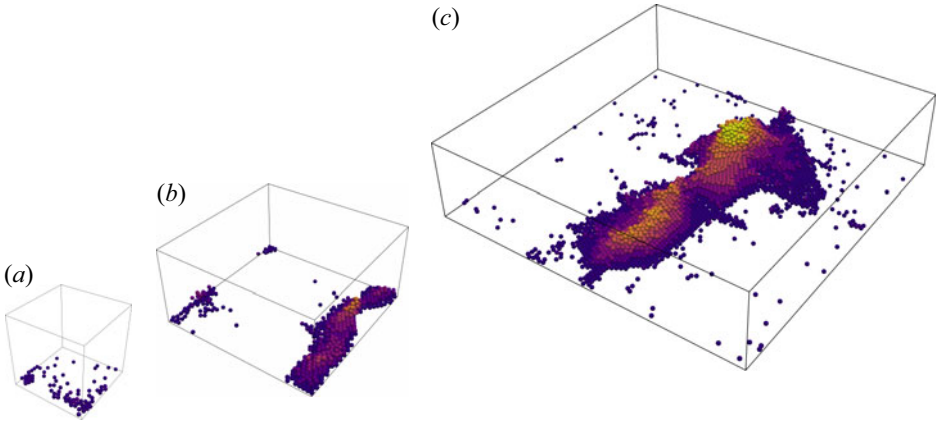


Figure 1. Snapshots of the configurations of sedimented particles for aspect ratios (*a*) $\Gamma = 1$ at $t^* = 50$, (*b*) $\Gamma = 2$ at $t^* = 70.1$ and (*c*) $\Gamma = 4$ at $t^* = 122.5$; colour indicates the particle height above the cell bottom. The times chosen are typical of configurations at steady state.

Examples of particle configurations close to steady state are shown in figure 1 for each aspect ratio. For clarity, only the particles that have sedimented on the bottom wall are shown. Particles are considered sedimented if they are in contact with the bottom wall directly or through a chain of contacts with other particles, at least one of which directly touches the bottom wall. A dune is defined as a group of connected particles that is in contact with the bottom wall. A union-find-based algorithm is used to efficiently identify particles belonging to the dunes, and to keep track of separate dunes. The details of this method can be found in Chen & Prosperetti (2024). Notably, the size of the dunes increases with the aspect ratio, as particles tend to cluster together and form a single large dune in larger domains while being more distributed in domains with smaller aspect ratios. Note that the particle distribution in larger aspect ratio domains is quite different from what might be expected by periodically extending the configurations of a smaller domain.

3.1. *Particle resuspension*

As described in greater detail in § 3.2, dunes form because the horizontal flow along the bottom of the cell, caused by the downward plumes, pushes the settled particles towards the base of the rising plumes, where they accumulate. As these particles maintain contact with the hot bottom wall, they heat up and localise the ascending plumes above the dune. By this process, in spite of their small volume fraction, the dunes are not a mere by-product of the circulation, but they play an important role in structuring the naturally convective flow in the domain. The fluid rising along the sides of the dunes drags the particles along their slopes and places them in the upward plumes detaching from the summit, thus enabling their entrainment and resuspension. Thus it is drag, rather than lift, that is ultimately responsible for the particle resuspension. The effectiveness of this mechanism is illustrated by figure 2, which displays the probability density function (PDF) of the normalised distance of the particle centres z_c/d_p above the cell base at the moment of resuspension. Particles are considered resuspended when they lose direct contact with the wall or a dune. A notable feature of this figure is the presence of oscillations with a period of approximately one particle diameter, which reflects the height of the dune-forming particle layers from which the particles detach when they undertake their upward motion. In the smallest cell, with $\Gamma = 1$, the PDF has a tall, narrow peak slightly above

https://doi.org/10.1017/jfm.2025.10451 Published online by Cambridge University Press

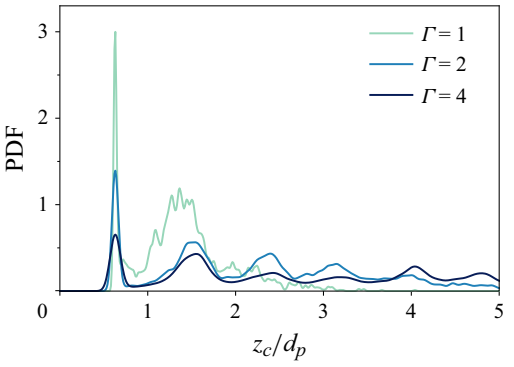


Figure 2. The PDF of the normalised particle height z_c/d_p above the cell base at the moment when they are resuspended, where z_c is the z coordinate of the particle centre.

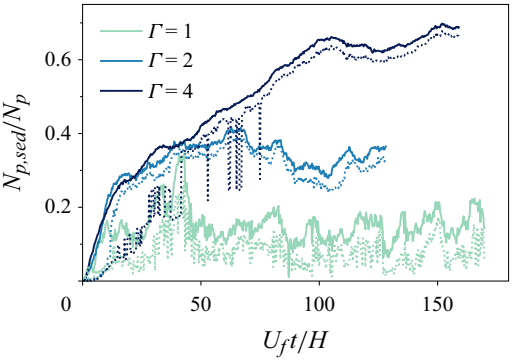


Figure 3. The number of sedimented particles $N_{p,sed}$, normalised by the total number of particles N_p, versus time (solid lines), for different aspect ratios in increasing order; the dotted lines are the normalised number of particles forming the biggest dune.

$d_p/2$, indicating that some particles start their ascent somewhat above the base. Since the number of these particles is proportional to the area under the peak, this effect is seen to play a minor role. Most particles start their rise for $d_p \lesssim z_c \lesssim 1.8\, d_p$, namely from layers one or two particle diameters thick. As Γ increases, the thin peak for $z_c/d_p < 1$ rapidly decreases while the PDF extends to many particle layers. The peaks for $\Gamma = 2$ are sufficiently sharp to permit a quantitative analysis that shows that their period is very close to $(\sqrt{3}/2)d_p$, which is the distance between the parallel planes passing through the centres of well-stacked spheres. This suggests that particles detach from the hollow formed by neighbouring spheres. For $\Gamma = 4$, the peaks are more smeared, given the less orderly dune structure that can form with many particles. These results provide a compelling proof of the significance of dunes in the resuspension process.

The size of the dunes can be quantified by comparing the number of sedimented particles $N_{p,sed}$, normalised by the total number of particles N_p, in figure 3; the solid lines show the total number of sedimented particles, and the dotted lines show the number of particles in the largest dune. Since $t = 0$ is the instant at which the particles kept fixed at random locations in the domain are released, $N_{p,sed}(t = 0) = 0$. With time, settling progresses until, in all cases, the lines appear to reach what may be approximately

https://doi.org/10.1017/jfm.2025.10451 Published online by Cambridge University Press

described as a statistically steady state. (Steady state may not have been quite attained for $\Gamma = 4$, but the trend towards a very large dune is nevertheless sufficiently clear from the results in this figure and in figure 1*c*.) The initial phase of dune build-up lasts for a considerably shorter time for the smaller aspect ratios: for $\Gamma = 1$, a steady state can be estimated to have been reached at approximately $t^* \sim 50$, for $\Gamma = 2$ at approximately $t^* \sim 70$, and for $\Gamma = 4$ at approximately $t^* \sim 100$. There are fluctuations of different magnitudes about the asymptotic state. In Chen & Prosperetti (2024), we have referred to the strong ones for $\Gamma = 1$ as 'breathing' to indicate the situation in which the dune appears to repeatedly condense and evaporate. The fluctuations are particularly strong in this case because, as explained below, resuspension is very effective for $\Gamma = 1$, and at the same time, flow fluctuations are particularly strong for small aspect ratios, as found in single-phase Rayleigh–Bénard simulations (see e.g. Stevens *et al.* 2018). The dunes for higher aspect ratios are more stable, experiencing smaller fluctuations after the initial transient. It is also evident that, all other parameters being kept constant, the normalised size of the dune is a strongly increasing function of the aspect ratio; an explanation of this fact will be provided later. For $\Gamma = 4$, the dotted line initially fails to track the solid line, but it catches up, showing only small differences. The implication is that with time, a progressively larger dune establishes itself by absorbing isolated smaller dunes to the point that, for $\Gamma = 4$, it ends up consisting of nearly 97 % of the total number of sedimented particles. The difference between the dotted and solid lines in figure 3 is greater for $\Gamma = 1$ than for the other aspect ratios, indicating that for the smallest aspect ratio, several other smaller dunes coexist with the largest one. For $\Gamma = 2$ and 4, one notices the sudden appearance of nearly vertical dotted lines, which indicates brief time intervals during which a 'crack' temporarily splits the largest dune into smaller ones that quickly re-merge.

The above observations raise key questions that the following sections will address. (i) Why does the system prefer a single, stable dune, and how does it form? (ii) How does the dune size depend on the system parameters? Section 3.2 focuses on the first question, and § 3.3 addresses the second question.

3.2. *Dune formation*

We now investigate in greater detail the process by which a large dune eventually forms, using the case $\Gamma = 4$ as an example. The snapshots of figure 4 illustrate the time evolution of the sedimented particles, with colour representing their height above the cell bottom. Figure 5 provides a top-down perspective, displaying both the particles and the fluid vertical velocity on a horizontal plane at height $1.25d_p$ above the bottom, corresponding to figures 4(*a*), 4(*b*) and 4(*c*). Initially, particles start to settle on the ground, with some giving rise to filaments, as illustrated in figure 6, which shows the vertical velocity on a horizontal plane $1.25d_p$ above the bottom wall together with vectors indicating the horizontal velocity of particles located between the plane and the bottom wall.

The formation of these filaments can be described as follows. When it reaches the proximity of the cell base, the fluid falling in descending plumes (such as the one marked with a purple box in figure 6) turns horizontally and pushes the particles that it encounters radially outwards. In this way, the stagnation points at the bottom of the downward plumes become repulsion points for the particle motion in the horizontal plane. The horizontal flow generated by a descending plume encounters similar flows generated by the neighbouring descending plumes. This interaction creates a series of points which, for reasons explained shortly, we call saddle points, at which the flow velocity along the line joining the stagnation points of two downward plumes vanishes. These saddle points are connected by lines, or filaments that, seen from below, give the impression of an irregularly

https://doi.org/10.1017/jfm.2025.10451 Published online by Cambridge University Press

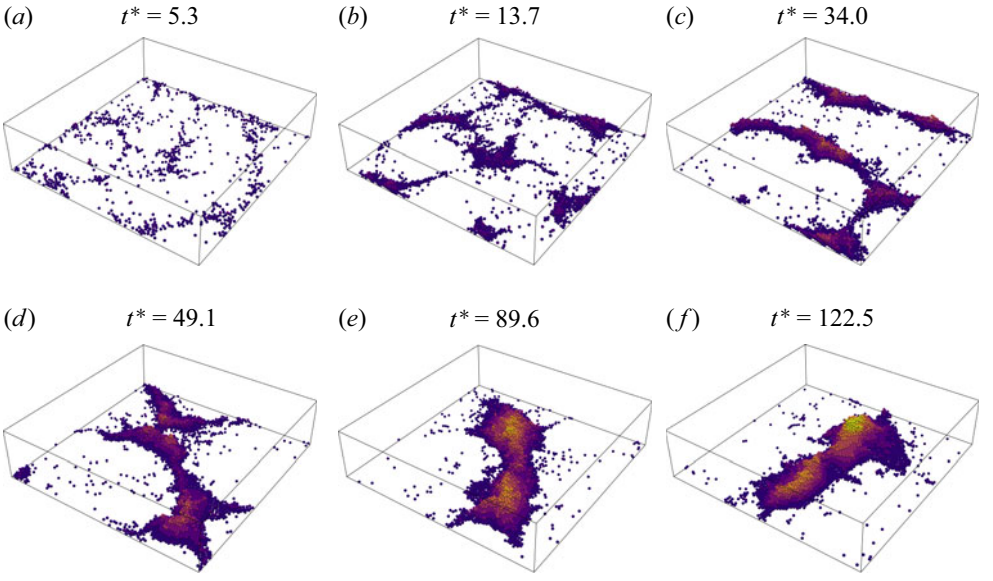


Figure 4. Sequence of snapshots documenting the evolution of the sedimented particles for $\Gamma = 4$; colour indicates the particle height above the cell bottom.

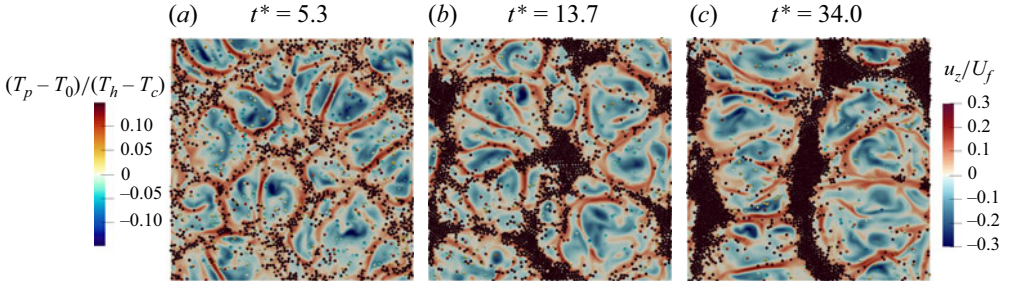


Figure 5. Top-down view of the fluid vertical velocity on a horizontal plane $1.25d_p$ above the bottom wall at three instants of time for the $\Gamma = 4$ simulation. The particles within the region between the plane and the bottom wall are also shown, coloured by their temperature.

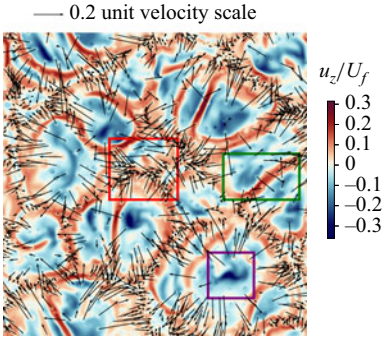


Figure 6. Top-down view of the fluid vertical velocity, indicated by colour, on a horizontal plane $1.25d_p$ above the bottom wall at $t^* = 5.3$ for $\Gamma = 4$. Arrows indicate the horizontal velocity vectors for all the particles within the region between the horizontal plane and the bottom wall. The red, green and purple boxes indicate attraction, saddle and repulsion regions; see text.

https://doi.org/10.1017/jfm.2025.10451 Published online by Cambridge University Press

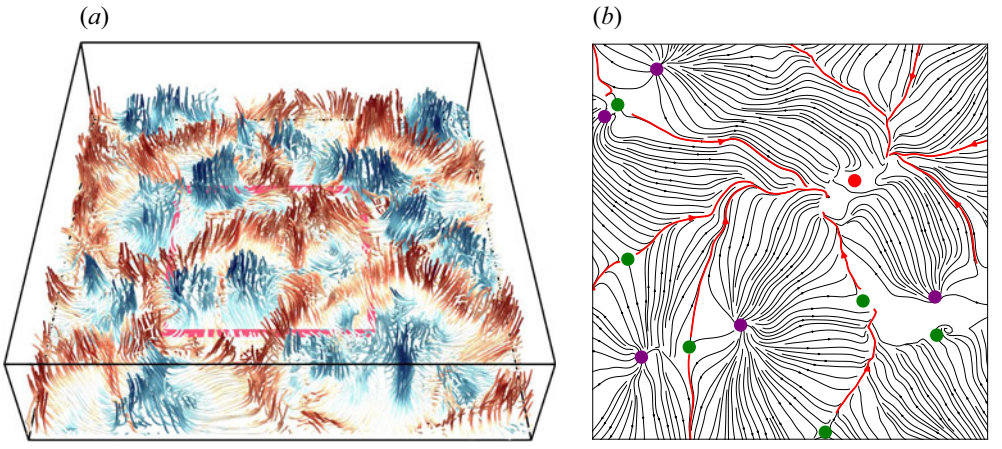


Figure 7. (*a*) Streamlines near the bottom wall coloured by vertical velocity at $t^* = 5.3$ for $\Gamma = 4$, red and blue indicating upward and downward plumes, respectively. (*b*) The two-dimensional streamlines in the region of the horizontal plane contained in the pink box (which is $1.25d_p$ above the bottom wall) are plotted with a top-down view. The purple, red and green dots represent the stagnation points of the downward plumes, attraction points and saddle points, respectively. The red streamlines show the pathways connecting the saddle points and the attraction points, and correspond to the thin rising plumes.

tessellated plane as shown in figure 5(*a*). As the fluid approaches these lines, it slows down due to its diverging nature and to the adverse pressure gradient, and heats up as it flows in contact with the warm base. In this way, the upward flow induced by the saddle points and generated along the lines that connect them is actually a thin warm rising plume (figure 7*a*). Along the bottom, particles are pushed by the flow towards the saddle points and the filaments, and are pushed along them on either side of the saddle points. This fact justifies our terminology as, insofar as the particle motion in the plane is concerned, they do behave as saddle points; an example can be seen inside the green box in figure 6. In this way, the filaments become pathways for the particle motion on the cell bottom, leading them to accumulate at attraction points where three or more filaments come together (red box in figure 6). Particles delivered to the attraction points jam there, accumulate, and form separate islands, or small dunes. This helps to localise the ascending plumes, further stabilising the attraction points and attracting new particles. This is the main mechanism leading to the rapid growth of the islands during the initial stage, as shown in figure 4(*b*), where the particles more or less follow the single-phase flow structures near the bottom wall. The repulsion points, saddle points, attraction points and pathways are illustrated in figure 7(*b*). Aside from the presence of the particles, the flow just described closely resembles the typical one observed in single-phase Rayleigh–Bénard convection (see e.g. Stevens *et al.* 2018). Initially, therefore, the particles do not alter the flow structure as might have been expected *a priori* given their relatively small amount.

At later times, however, particles do have a profound effect on the global flow, but for this to happen, the initial islands have to organise into large dunes. The first step in this evolution is the merging of isolated islands formed as just described. This process is driven by two factors, particle jamming and unequal plume strengths. First, as the islands grow due to continuous particle accumulation, their mutual separation decreases, shortening the particle pathways. Since they lie on the ground, the newly sedimented particles moving along the filaments can rarely, if ever, be resuspended before they reach the islands. If this process is too slow, then they will eventually clog the pathways and build a connection between neighbouring islands. This mechanism explains the linear extension of the dunes

https://doi.org/10.1017/jfm.2025.10451 Published online by Cambridge University Press

after the initial formation of separate islands that can be seen in the transition from figure 4(*b*) to figure 4(*c*); other examples of this process are visible in figure 5(*b*). In this way, the dunes continue to grow and merge into elongated structures.

Once the linear structures have formed, they can be pushed into each other, combining into even larger ones. This process can be caused simply by the 'wind' blowing along the cell bottom, or by a mechanism reminiscent of dune motion on the bottom of a river. Even though, unlike dunes on a river bottom, in the present flow the currents on both sides of a dune are directed from the base to the crest, there is a similarity if one of the two currents is stronger than the other, as the stronger stream would be able to push more particles in the direction of the weaker stream. Such mismatched plumes can be seen in figure 5(*c*), and they cause the two large ridges of particles to merge (figures 4*c,d*). The particles deep inside a large dune are exposed to negligible flow, and their mobility is severely reduced, a fact that enhances the stability of the dune. The only mobile particles are those on the dune surface, therefore the size and shape of the dune depend essentially on the effectiveness of the resuspension process. When this is weak, the dune can remain stable for a long time. Since the flow is turbulent, occasional strong bursts can appear and cause the temporary fracture of the dune, as shown in figure 3, but particles readily fall into the cracks, producing a single large dune again. A movie of the whole process of dune formation described here can be found in the supplementary movie here https://doi.org/10.1017/jfm.2025.10451.

The mechanism of dune formation is essentially the same for domains with smaller aspect ratios, including $\Gamma = 1$. What makes the details somewhat different in this case is the higher particle resuspension efficiency explained below. According to figure 3, the largest dunes in this case contain a few dozen particles, which rapidly accumulate into the structure. The stronger resuspension, however, gives the dune a very short lifetime because most of it quickly 'evaporates', the particles are resuspended, and the process must start anew (Chen & Prosperetti 2024).

3.3. *Boundary-layer thickness and particle diameter*

The size that the dunes reach at steady state reflects the statistical balance between the particle settling and resuspension rates. Let us start from a consideration of the latter. It was explained before that a key aspect of the physics of resuspension resides in the effectiveness with which the horizontal flow along the cell base is able to push the particles towards the dunes and up their slopes. This effectiveness must be the greater the more the particles stick out of the viscous boundary layer caused by the no-slip condition on the solid surfaces. On average, the distance the particles travel along the base of the cell is greater than the distance along the dune sides, therefore it makes sense to focus on the boundary layer formed at the cell bottom. It is known from the theory of single-phase Rayleigh–Bénard convection that this boundary layer behaves like a normal laminar boundary layer up to $Ra \sim 10^{14}$, at which point it turns turbulent, ushering in the so-called 'ultimate turbulent regime' (see e.g. Lohse & Shishkina 2024). It can therefore be safely assumed that at the Rayleigh numbers of our simulations, namely 10^7 and 10^8, the boundary layer is essentially laminar. Similarly to those of others (see e.g. du Puits *et al.* 2007; Shishkina & Thess 2009), our attempts to prove this fact from the numerical results have been inconclusive due primarily to flow unsteadiness, which in our case compounds with the complex geometry induced by the presence of particles. These features make it very difficult to calculate clean, uncontaminated average quantities. However, the single-phase particle image velocimetry data of Zhou *et al.* (2010) conclusively prove that the mean single-phase velocity profile agrees well with the theoretical Prandtl–Blasius profile.

https://doi.org/10.1017/jfm.2025.10451 Published online by Cambridge University Press

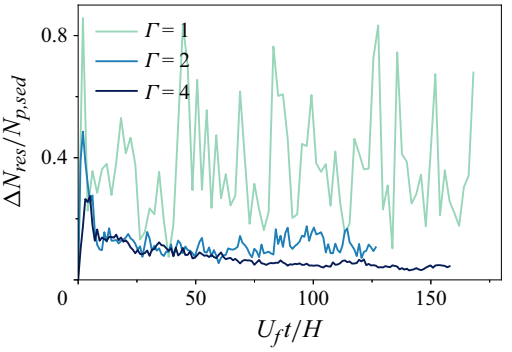


Figure 8. Here, ΔN_{res} is the number of particles resuspended during one time unit H/U_f. The time evolution of this quantity, normalised by the number of settled particles $N_{p,sed}$, is shown here for, in descending order, $\Gamma = 1, 2, 4$.

The situation has been reviewed in Zhou *et al.* (2010), who support this result beyond doubt. While all the evidence concerns single-phase flow, we feel justified in appealing to it because on the cell base, the particles are sparse, with a density far lower than average. Furthermore, as will be seen, the consequences that follow from this assumption are in very good agreement with the numerical results.

If the laminar nature of the boundary layer is accepted, then it follows that the horizontal scales of the flow near the cell bottom are proportional to L, so the thickness δ_v of the boundary layer can be estimated, up to a constant of order one, by the standard relation $\delta_v \sim L/\sqrt{LU_f/\nu_f}$. It is then straightforward to establish the relation

$$\frac{\delta_v}{d_p} \simeq \sqrt{\Gamma}\frac{H}{d_p}\left(\frac{Pr}{Ra}\right)^{1/4} = \sqrt{\Gamma}\frac{H}{d_p}\left(\frac{\nu_f^2}{\beta(T_h - T_c)gH^3}\right)^{1/4}. \tag{3.1}$$

In single-phase Rayleigh–Bénard convection at $Ra = 2 \times 10^7$, it is known that the scale of the largest flow structures at the cell mid-height keeps increasing until $\Gamma \sim 64$ (Stevens *et al.* 2018), but comparable information on the boundary-layer thickness is not available. All we can say on the basis of our experience (described below) is that the consequences of (3.1) are supported up to $\Gamma = 4$.

For the present simulations with $Ra = 10^7$, $H/d_p = 20$ and $\rho_p/\rho_0 = 1.1$, (3.1) becomes $\delta_v/d_p \simeq 0.36\,\Gamma^{1/2}$ and varies, therefore, from $\delta_v/d_p \simeq 0.36$ for $\Gamma = 1$, to $\delta_v/d_p \simeq 0.71$ for $\Gamma = 4$. In the smaller-aspect-ratio cell, therefore, most of the particle is outside the viscous boundary layer, while the opposite is true for the larger-aspect-ratio cell. One may therefore well expect a much greater resuspension efficiency for the smallest aspect ratio than for the largest one. This fact can be demonstrated by plotting the number of resuspended particles ΔN_{res} during a time unit $\tau_f = H/U_f$ normalised by the number of settled particles $N_{p,sed}$. These results are shown in figure 8 for $\Gamma = 1, 2, 4$. The line for $\Gamma = 1$ exhibits strong statistical fluctuations, which are a consequence both of the smaller number of particles and of the greater irregularity of the flow for this aspect ratio mentioned before. Although the line for $\Gamma = 4$ settles at a lower level than that for $\Gamma = 2$ as steady state is approached, the two nearly superpose until $U_f t/H \simeq 50$. An explanation of this feature is given below.

The previous interpretation is strengthened by a comparison of the normalised number of resuspended particles for $Ra = 10^7$ and 10^8 with $\Gamma = 2$. As already explained, the simulation at $Ra = 10^8$ was carried out by increasing the cell height, keeping all

https://doi.org/10.1017/jfm.2025.10451 Published online by Cambridge University Press

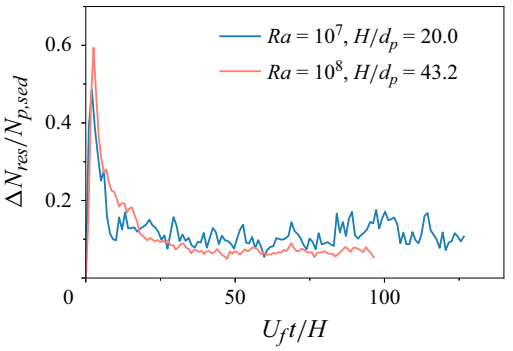


Figure 9. Temporal evolution of the number of particles resuspended during one time unit H/U_f, normalised by the number of settled particles $N_{p,sed}$, for $Ra = 10^7$,with $H/d_p = 20$, and $Ra = 10^8$ with $H/d_p = 43.2$.

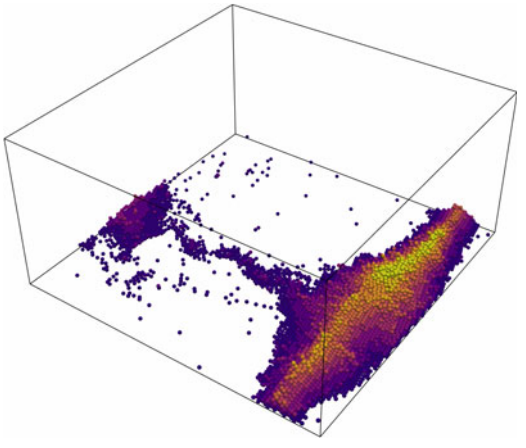


Figure 10. Particle configuration of sedimented particles for $Ra = 10^8$ and $\Gamma = 2$ at $t^* = 90.1$. Particles are coloured by their height above the cell base. Suspended particles are neglected in the plot.

other dimensional quantities at the same values as before. In particular, for this case, $H/d_p = 43.2$. For these conditions, (3.1) becomes $\delta_v/d_p \simeq 0.24(H/d_p)^{1/4}$ and therefore changes from $\delta_v/d_p \simeq 0.50$ for $Ra = 10^7$ and $H/d_p = 20$ to $\delta_v/d_p \approx 0.61$ for $Ra = 10^8$ and $H/d_p = 43.2$. The difference between the two situations is smaller than before and, indeed, the two normalised resuspensions are closer, as shown in figure 9. Remarkably, in spite of the increase of the Rayleigh number, which would lead one to expect a more vigorous resuspension and therefore a smaller fraction of sedimented particles, the opposite is found, in agreement with the prediction of (3.1). In this case, as can be seen in figure 10, the dune is indeed larger than that formed for $\Gamma = 2$ at $Ra = 10^7$ (figure 1*b*), and it has at least seven particle layers.

We now turn to the smaller-particle simulation for $Ra = 10^7$ and $\Gamma = 1$. In this case, (3.1) gives $\delta_v/d_p \simeq 0.018(H/d_p)$, namely $\delta_v/d_p \simeq 0.36$ and 0.509 for $H/d_p = 20$ and 28.3, respectively. The line for the former case is the same as that shown in figure 8 for $\Gamma = 1$. The difference between the two values of δ_v/d_p is comparable to that encountered earlier in the simulations for different aspect ratios, and as can be seen from figure 11, indeed there is a significant difference between the two simulations. The resuspension of the smaller particles is significantly weakened compared to that of the larger ones, with the consequence that the fluctuations of the dune size are much more moderate. As figure 12

https://doi.org/10.1017/jfm.2025.10451 Published online by Cambridge University Press

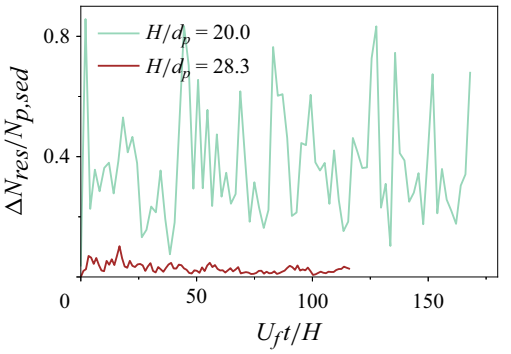


Figure 11. Temporal evolution of the number of particles resuspended during one time unit H/U_f, normalised by the number of settled particles $N_{p,sed}$, for normal-sized particles with $H/d_p = 20$, and smaller particles with $H/d_p = 28.3$. Here, $\Gamma = 1$ and $Ra = 10^7$.

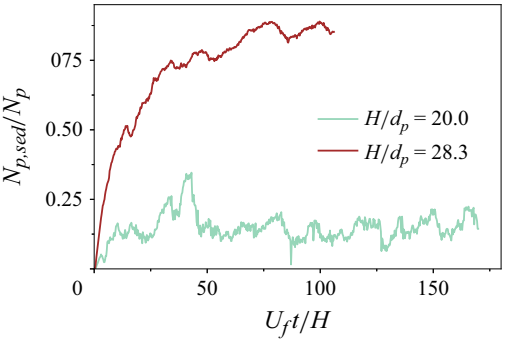


Figure 12. The number of sedimented particles normalised by the total number of particles, for smaller and normal-sized particles for $\Gamma = 1$.

shows, the dune is more stable and also contains a much greater fraction of particles than for $H/d_p = 20$. The greater mass fraction of the particles in this case may influence these results, but as shown in § 3.4, the effect is very minor.

It was noted in connection with figure 8 that the normalised numbers of resuspended particles for $Ra = 10^7$ and $\Gamma = 2, 4$ track each other until $U_f t/H \simeq 50$, at which point they deviate, with the resuspension for $\Gamma = 4$ becoming appreciably smaller than that for $\Gamma = 2$. This evolution can also be looked at from a different angle by considering the normalised number of particles deposited during a time unit τ_f, which is shown in figure 13. Here, we see that the curves for the two aspect ratios are very close to each other up to $U_f t/H \sim 50$, but then start diverging. An explanation of these features suggests itself if we look at the particle and flow arrangements before and after this time. Figure 14(a) shows, for $\Gamma = 4$, an instantaneous image of the arrangement of particles with $(T_p - T_0)/(T_h - T_c) \geqslant 0.125$ at $U_f t/H = 30.1$. Being relatively warm, the majority of these particles rest on the cell bottom. Figure 14(b) shows the fluid streamlines averaged over the time interval $23.8 \leqslant U_f t/H \leqslant 36.5$, coloured by the local vertical velocity. It can be seen that the settled particles are mostly arranged into two dunes, and the flow is correspondingly arranged in two recirculating flow structures separated by a distance approximately equal to half the cell, i.e. $2H$. In this sense, the situation is similar to the $\Gamma = 2$ case, as can be seen from figures 15(a) and 15(b), and indeed, the entrainment and

https://doi.org/10.1017/jfm.2025.10451 Published online by Cambridge University Press

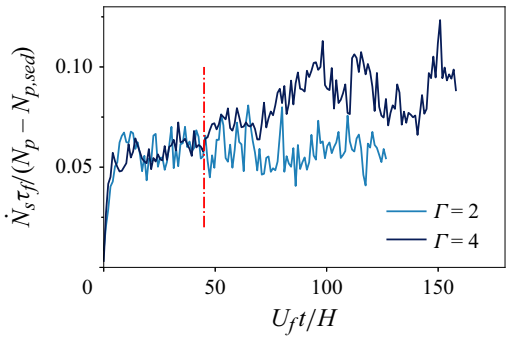


Figure 13. Number of suspended particles settling during one time unit H/U_f normalised by the number of suspended particles versus time for aspect ratios $\Gamma = 2, 4$. The vertical red dash-dotted line at $t^* = 45$ indicates the time at which the two elongated dunes visible at time $U_f t/H = 34.0$ in figure 4(*c*) begin to merge into a single dune spanning the diagonal of the domain for $\Gamma = 4$.

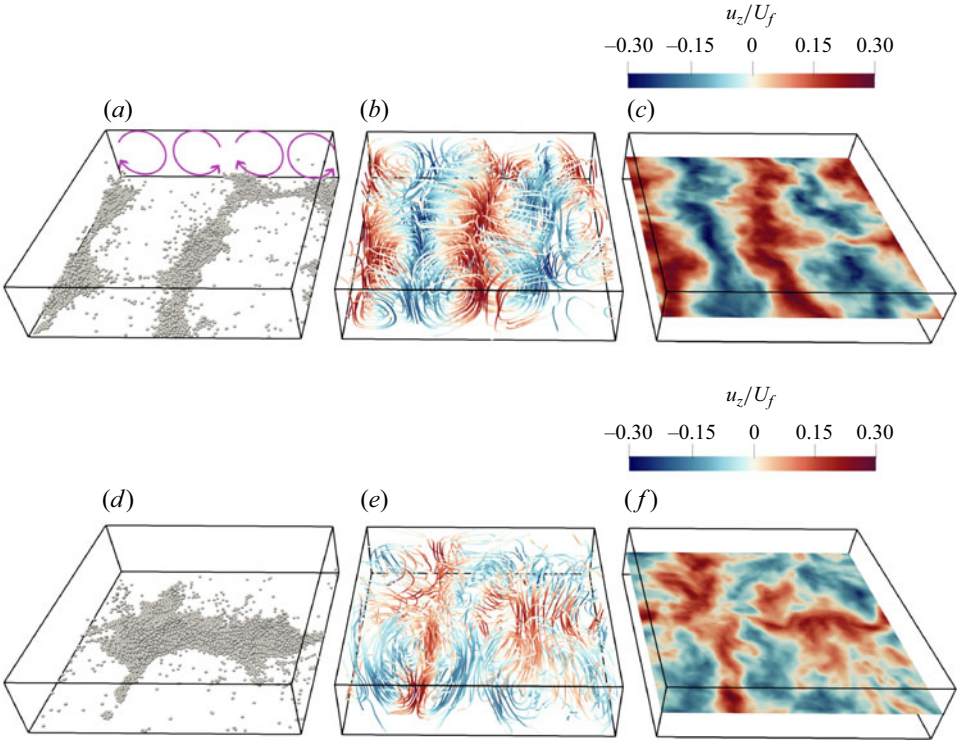


Figure 14. (*a*) Warm particles with $(T_p - T_0)/(T_h - T_c) > 0.125$ at $t^* = 30.13$. (*b*) Streamlines coloured by the vertical velocity. (*c*) Mid-height vertical velocity, time-averaged over $23.8 \leqslant t^* \leqslant 36.5$. (*d*) Warm particles with $(T_p - T_0)/(T_h - T_c) > 0.125$ at $t^* = 116.2$. (*e*) Streamlines coloured by the vertical velocity. (*f*) Mid-height vertical velocity, time-averaged over $109.9 \leqslant t^* \leqslant 122.5$. Here, $\Gamma = 4$.

deposition rates for the two aspect ratios are very close. Note that what we see in the $\Gamma = 4$ cell is not the periodic repetition of the $\Gamma = 2$ one, but the break-up of the flow into two approximately rectangular cells, with length $4H$ in the direction parallel to the dunes, and $\sim 2H$ in the transverse direction. In this situation, the average length of the particle path along the cell base towards the dunes is comparable to that of the particles in the $\Gamma = 2$

https://doi.org/10.1017/jfm.2025.10451 Published online by Cambridge University Press

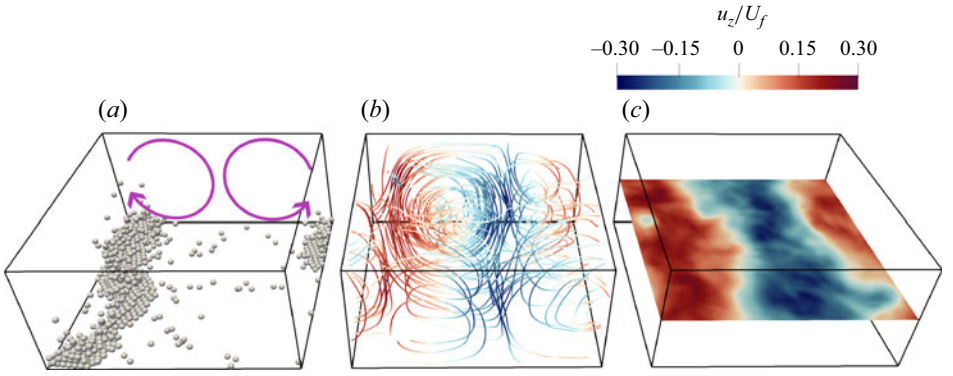


Figure 15. (*a*) Warm particles with $(T_p - T_0)/(T_h - T_c) > 0.125$ at $t^* = 75.2$. (*b*) Streamlines coloured by the vertical velocity, time-averaged over $68.9 \leqslant t^* \leqslant 81.5$. (*c*) Time-averaged mid-height vertical velocity. Here, $\Gamma = 2$.

case. It is only later that the two dunes of the $\Gamma = 4$ simulation start to merge (figures 4*d,e*), and at this point, the average horizontal particle path doubles and, according to (3.1), the boundary layer thickens and the resuspension becomes less effective.

Figure 13 shows that near $U_f t/H \sim 50$, when the two dunes of the $\Gamma = 4$ simulation merge, the number of settling relative to suspended particles increases so that the necessary balance with the decreased fraction of resuspended particles shown in figure 8 is ensured. (Note that this statement concerns the relative, not absolute, numbers of both types of particles, which actually decrease as the dune size increases.) This increase of the fraction of settling particles can be imputed to a decreased coherence of the flow structures, which is evident when comparing the streamlines in figure 14. A similar point was made by Marsh & Maxey (1985) and Martin & Nokes (1989). By means of a simple model of particles settling in steady, cellular convection, the former authors found that a large proportion of particles could remain suspended indefinitely, and argued that the addition of turbulent fluctuations to such a flow would reduce the proportion of particles that could remain suspended indefinitely. Martin & Nokes (1989) also argued that all particles would eventually deposit on the bottom in an incoherent flow.

The streamlines of figure 14 are not the only indication of the eventual loss of coherence of the flow for $\Gamma = 4$. This fact is confirmed and strengthened by a consideration of the correlation coefficients between the mid-height vertical velocity and the temperature near the cell bottom for $\Gamma = 2, 4$, shown in figure 16. A large value of this coefficient would indicate that plumes rise/sink fairly rectilinearly above positions of high/low bottom temperature, but both these coefficients start at a low value at early times. This result indicates that these early-time plumes (which figures 4(*a*) and 5(*a*) show to be irregularly distributed with hardly any dunes at $U_f t/H = 5.4$) are relatively weak and easily deviated in their ascent/descent. The correlation increases at $U_f t/H = 13.7$, at which point a number of well-formed dunes can be seen in figures 4(*b*) and 5(*b*), and reaches a maximum at approximately $U_f t/H = 34$, a time at which figures 4(*c*) and 5(*c*) show two large dunes. The relatively large value of the correlation coefficient reached at these times suggests that the plumes are strong and well developed. Past $U_f t/H \sim 50$, however, the coefficient for $\Gamma = 4$ starts deviating from that for $\Gamma = 2$, decreasing to a much lower value. Whether this is due to a weakening of the plume caused by the greater height of the dune, which makes its top cooler due to the relative inefficiency of conduction, or by the onset of horizontal convection in the cell, which strongly tilts and disrupts the plumes in their ascent/descent,

https://doi.org/10.1017/jfm.2025.10451 Published online by Cambridge University Press

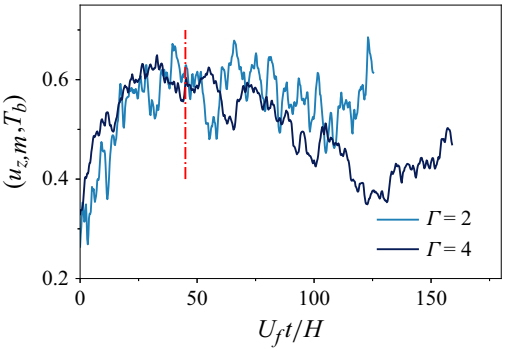


Figure 16. Time evolution of the correlation coefficient between the mid-height vertical velocity field $u_{z,m}$ and the temperature field T_b on a horizontal plane near $1.25d_p$ above the cell bottom, denoted as $(u_{z,m}, T_b)$, for $\Gamma = 2, 4$. The red dash-dotted line at $t^* = 45$ indicates when the two elongated dunes merge into a single dune spanning the diagonal of the domain for $\Gamma = 4$.

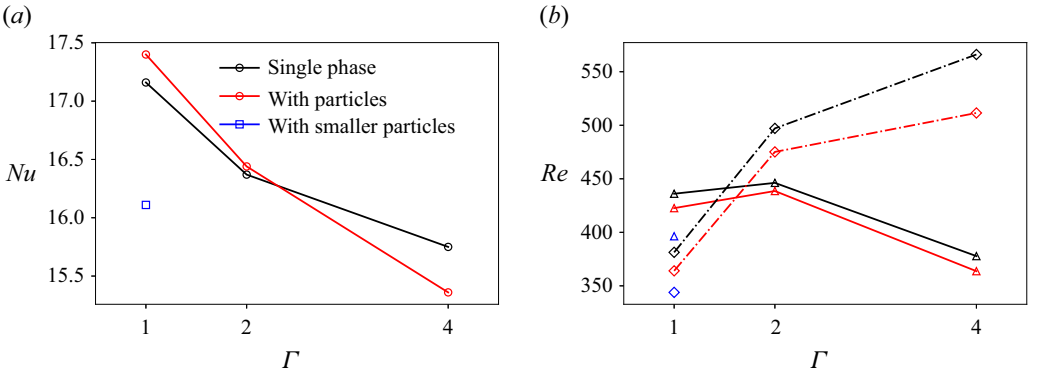


Figure 17. (*a*) The Nusselt number Nu and (*b*) the Reynolds number Re, versus aspect ratio, both with and without particles. The single-phase results are shown in black. Red and blue lines represent particulate flows with $Ra = 10^7$ and $H/d_p = 20.0$, and $Ra = 10^7$ and $H/d_p = 28.3$, respectively. In (*b*), solid lines with triangles represent the vertical Reynolds number, and dash-dotted lines with diamonds represent the horizontal Reynolds number.

it is not possible to say with assurance. In any event, in either case, the flow is disrupted and becomes more irregular, with the consequence that particle settling is favoured.

3.4. *Nusselt and Reynolds numbers*

Although not the focus of this study, it is also of interest to present results for the Nusselt and Reynolds numbers of the flow in the cell. Figure 17(*a*) collects the present results for the Nusselt number for single-phase flow (circles) and for the two-phase simulations with $Ra = 10^7$. The single-phase results exhibit the same decreases with increasing aspect ratio found by other investigators (see e.g. Stevens *et al.* 2018). The larger particles, with $H/d_p = 20$, cause a slight increase for $\Gamma = 1$, a slight decrease for $\Gamma = 4$, and a negligible difference for $\Gamma = 2$. The $\Gamma = 1$ result reproduces that of our earlier study (see e.g. Chen & Prosperetti 2024), which was imputed to the fact that, unlike a fluid parcel that is broken up by the surrounding fluid in its ascent, particles maintain their integrity and are therefore able to carry their thermal energy all the way to the top of the cell. The smaller particles with $H/d_p = 28.3$, on the other hand, are seen to decrease the Nusselt number somewhat

https://doi.org/10.1017/jfm.2025.10451 Published online by Cambridge University Press

with respect to the single-phase result, in spite of the fact that they have the same terminal Reynolds number and occupy the same fraction of the total volume. This negative effect is probably due to the particle mass fraction, which is approximately 16 % greater than for the larger particles. It is true that, according to figure 12, the fraction of small suspended particles is approximately five times smaller than that of the larger particles, but their total number is three times as large, so even counting only the suspended particles, a net mass fraction increase still results.

Different definitions are possible for the Reynolds number in the cell. Here, we define a horizontal Reynolds number $Re_h = (\sqrt{\langle u_x^2\rangle + \langle u_y^2\rangle}\, H)/\nu_f$ and a vertical Reynolds number $Re_v = (\sqrt{\langle u_z^2\rangle}\, H)/\nu_f$, with the angle brackets indicating a volume average. Our computed results for single- and two-phase Rayleigh–Bénard convection for the larger particles with $H/d_p = 20$ at $Ra = 10^7$ are shown in figure 17(*b*), with diamonds and triangles indicating the horizontal and vertical Reynolds numbers. The trends are the same as those found in the literature for the single-phase case, with Re_h an increasing function of Γ, and Re_v nearly independent of Γ up to $\Gamma = 2$, and decreasing for $\Gamma = 4$. The contrasting trends of Re_h and Re_v suggest that the vertical ascent/descent of the plumes is disrupted by an increasing horizontal flow, which agrees with the remarks made earlier in connection with figure 16, and the decline of the Nusselt number for $\Gamma = 4$ seen in figure 17(*a*). For the smaller particles with $H/d_p = 28.3$, the flow is slowed down for the reason explained before, and both Reynolds numbers are found to be smaller.

The results for our single simulation with $Ra = 10^8$ cannot be shown in figure 17 without an undesirable compression of the vertical scale, and we prefer to quote numerical results. The single- and two-phase Nusselt numbers are approximately 31.3 and 30.7. Since $\Gamma = 2$ in this simulation, the situation is therefore seen to be very similar to that shown in figure 17(*a*) for this aspect ratio. The horizontal Reynolds numbers are approximately 1446 and 1480 for single- and two-phase flow, respectively, while the vertical ones are approximately 1213 and 1285.

4. Summary and conclusions

This paper reports the results of a numerical study of Rayleigh–Bénard convection with suspended particles slightly heavier than the fluid. Our results have implications for crystallisation in magmas and lava lakes, solidification of metal melts, atmospheric flows, particle transport in the built environment, and others. A remarkable point is that even at the small volume fraction that we study, approximately 3.3 %, the dunes can completely reorganise the flow, determining the number and location of the convective cells. The effect on the Nusselt number and the Reynolds number of the flow remains, however, small (§ 3.4).

By accounting for the finite size of the particles, we show how the very nature of the convective flow causes them to accumulate into dunes, which play a crucial role in resuspension and in the maintenance of a statistically steady state (§ 3.2). The entrainment mechanism that we describe agrees very well with that discovered by Solomatov *et al.* (1993) in their experiments on sand in water, and sheds additional light on its nature. The role of dunes in promoting the suspension and entrainment of stones on the bottom of river beds has long been appreciated, but a crucial difference with our case is that in Rayleigh–Bénard convection, turbulent stresses are not an essential part of the entrainment process.

https://doi.org/10.1017/jfm.2025.10451 Published online by Cambridge University Press

A major component of the resuspension mechanism is the entrainment of particles settled on the ground by the near-ground horizontal flow produced by the descending plumes. This flow accumulates the particles near a number of attraction points, forming small islands that, in time, merge into bigger dunes. When the horizontal flow meets a dune, it is deviated upwards along its slopes and pushes particles to the dune top where the upward plumes develop. The particles get resuspended by being entrained in this upward flow. Thus drag, rather than lift, is the essence of the resuspension mechanism. In the parameter range that we have explored, direct resuspension from the cell base, if it happens at all, is exceedingly rare (§ 3.1). At steady state, the size of the dunes is determined by a balance between settling and resuspension. Since very little resuspension can take place without dunes, it follows that at most very few particles can remain suspended in the flow if dune formation is hindered.

Efficiency of the resuspension process is therefore a crucial ingredient for the maintenance of a two-phase flow. The fundamental ingredient of this process is the drag force exerted by the fluid, which moves a settled particle first along the cell bottom and then up a dune slope. Viscous boundary layers develop along these boundaries, and the drag force on the particles is the smaller the deeper they are immersed in this thin region of viscous flow. The ratio δ_v/d_p of the boundary-layer thickness δ_v to the particle diameter d_p therefore becomes the key parameter determining the resuspension efficiency, the dune size, and the number and fraction of suspended particles (§ 3.3). Equation (3.1) gives an estimate of this parameter in terms of the cell aspect ratio, the ratio of the cell height to the particle diameter, and the Rayleigh and Prandtl numbers. The major computational requirements of our simulations have prevented us from carrying out a detailed study of the parameter space, but we have shown that the dune size increases with the cell aspect ratio and as the particle size is made smaller, just as predicted by the equation. Interestingly, we also found that increasing the Rayleigh number Ra does not necessarily increase the resuspension rate if Ra is increased in such a way that δ_v/d_p decreases.

In all of our simulations, a single large dune emerges with time until, at steady state, the largest linear dimension of its footprint becomes comparable to that of the cell base. It would be interesting to know whether this trend extends to larger aspect ratios. It is possible that higher Rayleigh numbers cause increasingly turbulent flow that might break up larger dunes into a number of smaller ones. The settling of suspended particles would also be strongly affected by increased turbulence, which would have an influence on the suspension/settling balance on which the dunes depend. The resuspension of very small particles might require very intense turbulence and might lead to entrainment by a Shields mechanism, in addition to the entrainment by upward plumes that we have elucidated. It is difficult to predict the outcome of the interaction among these diverse processes as the Rayleigh number and aspect ratio are increased. Progress on these issues must await further work, computational and possibly experimental.

Supplementary movie. Supplementary movie is available at https://doi.org/10.1017/jfm.2025.10451.

Acknowledgements. The authors acknowledge the use of the Carya cluster and are grateful to Dr J. Ebalunode of the University of Houston Research Computing Data Core for his support.

Funding. This study was supported in part by the National Science Foundation CBET TTP programme under grant no. 2053204. This research used resources of the Oak Ridge Leadership Computing Facility at the Oak Ridge National Laboratory, which is supported by the Office of Science of the US Department of Energy under contract no. DE-AC05-00OR22725.

Declaration of interests. The authors report no conflict of interest.

https://doi.org/10.1017/jfm.2025.10451 Published online by Cambridge University Press

Data availability statement. The data that support the findings of this study are available from the corresponding author upon reasonable request.

References

Ahlers, G., Grossmann, S. & Lohse, D. 2009 Heat transfer and large scale dynamics in turbulent Rayleigh–Bénard convection. *Rev. Mod. Phys.* **81**, 503–537.

Auta, H.S., Emenike, C.U. & Fauziah, S.H. 2017 Distribution and importance of microplastics in the marine environment: a review of the sources, fate, effects, and potential solutions. *Environ. Intl* **102**, 165–176.

Balachandar, S., Zaleski, S., Soldati, A., Ahmadi, G. & Bourouiba, L. 2020 Host-to-host airborne transmission as a multiphase flow problem for science-based social distance guidelines. *Intl J. Multiphase Flow* **132**, 103439.

Bergman, T.L., Lavine, A.S., Incropera, F.P. & DeWitt, D.P. 2018 *Fundamentals of Heat and Mass Transfer*, 8th edn. Wiley.

Best, J. 2005 The fluid dynamics of river dunes: a review and some future research directions. *J. Geophys. Res. Earth* **110** (F4), F04S02.

Chen, X., Ostilla Monico, R., Floryan, D. & Prosperetti, A. 2024 Particle re-suspension in two-phase dispersed Rayleigh–Bénard convection. arXiv:2410.02886.

Chen, X. & Prosperetti, A. 2024 Particle-resolved multiphase Rayleigh–Bénard convection. *Phys. Rev. Fluids* **9** (5), 054301.

Clift, R., Grace, J. & Weber, M. 1978 *Bubbles, Drops, and Particles*. Academic Press.

Cózar, A. *et al.* 2017 The Arctic Ocean as a dead end for floating plastics in the North Atlantic branch of the thermohaline circulation. *Sci. Adv.* **3** (4), e1600582.

Demou, A.D., Ardekani, M.N., Mirbod, P. & Brandt, L. 2022 Turbulent Rayleigh–Bénard convection in non-colloidal suspensions. *J. Fluid Mech.* **945**, A6.

Elkins-Tanton, L.T. 2012 Magma oceans in the inner solar system. *Annu. Rev. Earth Planet. Sci.* **40**, 113–139.

Engelund, F. & Fredsøe, J. 1982 Sediment ripples and dunes. *Annu. Rev. Fluid Mech.* **14** (1), 13–37.

Fry, B., Lacaze, L., Bonometti, T., Elyakime, P. & Charru, F. 2024 From discrete to continuum description of weakly inertial bedload transport. *Phys. Rev. Fluids* **9** (2), 024304.

Gereltbyamba, B. & Lee, C. 2018 Behavior of settling inertial particles in a differentially heated cubic cavity at moderate Rayleigh number. *J. Mech. Sci. Technol.* **32**, 3169–3182.

Gu, J.C., Takeuchi, S. & Kajishima, T. 2018 Influence of Rayleigh number and solid volume fraction in particle-dispersed natural convection. *Intl J. Heat Mass Transfer* **120**, 250–258.

Jarvis, R.A. & Woods, A.W. 1994 The nucleation, growth and settling of crystals from a turbulently convecting fluid. *J. Fluid Mech.* **273**, 83–107.

Kidanemariam, A.G. & Uhlmann, M. 2014 Interface-resolved direct numerical simulation of the erosion of a sediment bed sheared by laminar channel flow. *Intl J. Multiphase Flow* **67**, 174–188.

Kok, J.F., Parteli, E.J., Michaels, T.I. & Karam, D.B. 2012 The physics of wind-blown sand and dust. *Rep. Prog. Phys.* **75** (10), 106901.

Krug, D., Lohse, D. & Stevens, R.J. 2020 Coherence of temperature and velocity superstructures in turbulent Rayleigh–Bénard flow. *J. Fluid Mech.* **887**, A2.

Lavorel, G. & Le Bars, M. 2009 Sedimentation of particles in a vigorously convecting fluid. *Phys. Rev. E.* **80**, 046324.

Lee, M. 2024 Spectral analysis of the correlation between temperature and wall-normal velocity in Rayleigh–Bénard convection at moderate Rayleigh numbers. *J. Phys.: Conf. Ser.* **2753**, 012006.

Lohse, D. & Shishkina, O. 2024 Ultimate Rayleigh–Bénard turbulence. *Rev. Mod. Phys.* **96**, 035001.

Marsh, B.D. & Maxey, M.R. 1985 On the distribution and separation of crystals in convecting magma. *J. Volcanol. Geotherm. Res.* **24** (1–2), 95–150.

Martin, D. & Nokes, R. 1989 A fluid-dynamical study of crystal settling in convecting magmas. *J. Petrol.* **30**, 1471–1500.

Oresta, P., Fornarelli, F. & Prosperetti, A. 2014 Multiphase Rayleigh–Bénard convection. *Mech. Eng. Rev.* **1**, FE0003.

Oresta, P. & Prosperetti, A. 2013 Effects of particle settling on Rayleigh–Bénard convection. *Phys. Rev. E.* **87**, 063014.

Park, H.J., O'Keefe, K. & Richter, D.H. 2018 Rayleigh–Bénard turbulence modified by two-way coupled inertial, nonisothermal particles. *Phys. Rev. Fluids* **3**, 034307.

Patočka, V., Calzavarini, E. & Tosi, N. 2020 Settling of inertial particles in turbulent Rayleigh–Bénard convection. *Phys. Rev. Fluids* **5**, 114304.

https://doi.org/10.1017/jfm.2025.10451 Published online by Cambridge University Press

DU PUITS, R., RESAGK, C., TILGNER, A., BUSSE, F. & THESS, A. 2007 Structure of thermal boundary layers in turbulent Rayleigh–Bénard convection. *J. Fluid Mech.* **572**, 231–254.

PURAGLIESI, R., DEHBI, A., LERICHE, E., SOLDATI, A. & DEVILLE, M.O. 2011 DNS of buoyancy-driven flows and Lagrangian particle tracking in a square cavity at high Rayleigh numbers. *Intl J. Heat Fluid Flow* **32**, 915–931.

PYE, K. & TSOAR, H. 2009 *Aeolian Sand and Sand Dunes*. Springer.

RANZ, W.E. & MARSHALL, W.R. 1952 Evaporation from drops. *Chem. Engng Prog.* **48**, 141–146.

RAYEGAN, S., SHU, C., BERQUIST, J., JEON, J., ZHOU, L., WANG, L.Z., MBARECHE, H., TARDIF, P. & GE, H. 2023 A review on indoor airborne transmission of COVID-19 – modelling and mitigation approaches. *J. Build. Engng* **64**, 105599.

SHISHKINA, O. 2021 Rayleigh–Bénard convection: the container shape matters. *Phys. Rev. Fluids* **6** (9), 090502.

SHISHKINA, O. & THESS, A. 2009 Mean temperature profiles in turbulent Rayleigh–Bénard convection of water. *J. Fluid Mech.* **633**, 449–460.

SIERAKOWSKI, A.J. & PROSPERETTI, A. 2016 Resolved-particle simulation by the Physalis method: enhancements and new capabilities. *J. Comput. Phys.* **309**, 164–184.

SOLOMATOV, V.S., OLSON, P. & STEVENSON, D.J. 1993 Entrainment from a bed of particles by thermal convection. *Earth Planet. Sci. Lett.* **120**, 387–393.

STEIN, A.F., DRAXLER, R.R., ROLPH, G.D., STUNDER, B.J.B., COHEN, M.D. & NGAN, F. 2015 NOAA's HYSPLIT atmospheric and dispersion modeling system. *Bull. Am. Meteorol. Soc.* **96**, 2059–2077.

STEVENS, R.J., BLASS, A., ZHU, X., VERZICCO, R. & LOHSE, D. 2018 Turbulent thermal superstructures in Rayleigh–Bénard convection. *Phys. Rev. Fluids* **3** (4), 041501.

TAKEUCHI, S., TSUTSUMI, T., KONDO, K., HARADA, T. & KAJISHIMA, T. 2015 Heat transfer in natural convection with finite-sized particles considering thermal conductance due to inter-particle contacts. *Comput. Therm. Sci.* **7**, 385–404.

VOWINCKEL, B., BIEGERT, E., MEIBURG, E., AUSSILLOUS, P. & GUAZZELLI, É. 2021 Rheology of mobile sediment beds sheared by viscous, pressure-driven flows. *J. Fluid Mech.* **921**, A20.

WANG, Y., SIERAKOWSKI, A.J. & PROSPERETTI, A. 2017 Fully-resolved simulation of particulate flows with particles–fluid heat transfer. *J. Comput. Phys.* **3**, 638–656.

WU, H., KARZHAUBAYEV, K., SHEN, J. & WANG, L.P. 2024 Direct numerical simulation of three-dimensional particle-laden thermal convection using the lattice Boltzmann method. *Comput. Fluids* **276**, 106268.

ZHOU, Q., STEVENS, R.J., SUGIYAMA, K., GROSSMANN, S., LOHSE, D. & XIA, K. 2010 Prandtl–Blasius temperature and velocity boundary-layer profiles in turbulent Rayleigh–Bénard convection. *J. Fluid Mech.* **664**, 297–312.

https://doi.org/10.1017/jfm.2025.10451 Published online by Cambridge University Press